









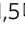


Observation of anomalous amplitude modes in the kagome metal CsV_3Sb_5

Gan Liu¹, Xinran Ma¹, Kuanyu He¹, Qing Li¹ , Hengxin Tan², Yizhou Liu² , Jie Xu¹, Wenna Tang¹, Kenji Watanabe³ , Takashi Taniguchi⁴ , Libo Gao^{1,5} , Yaomin Dai^{1,5} , Hai-Hu Wen^{1,5} , Binghai Yan²   & Xiaoxiang Xi^{1,5}  

The kagome lattice provides a fertile platform to explore novel symmetry-breaking states. Charge-density wave (CDW) instabilities have been recently discovered in a new kagome metal family, commonly considered to arise from Fermi-surface instabilities. Here we report the observation of Raman-active CDW amplitude modes in CsV_3Sb_5 , which are collective excitations typically thought to emerge out of frozen soft phonons, although phonon softening is elusive experimentally. The amplitude modes strongly hybridize with other superlattice modes, imparting them with clear temperature-dependent frequency shift and broadening, rarely seen in other known CDW materials. Both the mode mixing and the large amplitude mode frequencies suggest that the CDW exhibits the character of strong electron-phonon coupling, a regime in which phonon softening can cease to exist. Our work highlights the importance of the lattice degree of freedom in the CDW formation and points to the complex nature of the mechanism.

¹National Laboratory of Solid State Microstructures and Department of Physics, Nanjing University, Nanjing 210093, China. ²Department of Condensed Matter Physics, Weizmann Institute of Science, Rehovot 7610001, Israel. ³Research Center for Functional Materials, National Institute for Materials Science, 1-1 Namiki, Tsukuba 305-0044, Japan. ⁴International Center for Materials Nanoarchitectonics, National Institute for Materials Science, 1-1 Namiki, Tsukuba 305-0044, Japan. ⁵Collaborative Innovation Center of Advanced Microstructures, Nanjing University, Nanjing 210093, China. ✉email: binghai.yan@weizmann.ac.il; xxi@nju.edu.cn

Materials with a kagome lattice can host rich phenomena encompassing quantum magnetism^{1,2}, Dirac fermions^{3,4}, nontrivial topology^{5–7}, density waves, and superconductivity^{8–10}. The recently discovered kagome metals AV_3Sb_5 ($A = K, Rb, \text{ or } Cs$)^{11,12} offer a new platform to study the interplay of these phenomena. These compounds have Fermi levels close to Dirac points or van Hove singularities^{12–14}, leading to a plethora of possible intriguing ground states. Indeed, charge-density waves and superconductivity have been discovered^{12,15,16}, with ample evidence showing that both types of orders are exotic. For example, the CDW transition is accompanied possibly by a large anomalous Hall effect^{17,18}, and the superconductivity features a pair-density wave state¹⁹.

The nature of the CDW state and the mechanism for its formation have been under close scrutiny. In this work, we focus on CsV_3Sb_5 , which has a CDW transition temperature $T_{CDW} = 94 \text{ K}$ ¹². Both hard-X-ray and neutron scattering showed the lack of soft phonons (phonon modes that show frequency softening upon cooling toward a phase transition)^{20,21}, although density functional theory (DFT) calculations found two phonon instabilities at the M and L points of the Brillouin zone^{22–24}. Considering that a 2×2 modulation of the crystal lattice is well established^{12,19,25–27}, the absence of soft modes apparently breaks a pattern proven generic to many known CDW systems—a soft phonon freezes to zero frequency and triggers the formation of a distorted lattice²⁸. Currently, there is still no consensus on the form of the in-plane structure and the c -axis periodicity^{27,29}. The roles of Fermi-surface nesting and electron–phonon coupling are also debated. Because the period of the 2×2 superlattice matches perfectly with the Fermiology of the van Hove singularity, it is natural to ascribe the CDW transition to Fermi surface nesting^{22,30–32}, supported by the appreciable partial gapping of the Fermi surface observed experimentally^{33–37}. However, the calculated electronic susceptibility lacks the expected divergence^{38,39}, and the effect of electron–phonon coupling may not be dismissed^{21,39}.

Because the CDW features lattice distortions, studies of the lattice degree of freedom can offer insight into the mechanism. Raman scattering is a valuable tool in this respect. In well-studied CDW systems, such as the transition metal dichalcogenides, as a soft phonon mode condenses to form a distorted lattice, new Raman-active collective excitations, known as amplitude modes, emerge, providing a direct probe of the CDW order parameter^{40–42} (see Fig. 1a). Conversely, the observation of amplitude modes is typically considered as evidence for the soft mode. The temperature dependence of the amplitude modes as well as the zone-folded modes, which become Raman-active due to zone folding induced by the superlattice, can both reflect the CDW transition^{43–49}. Combined with symmetry information from polarization-resolved measurements, constraints can be set on the possible CDW ground state.

Here, we report Raman scattering measurements on CsV_3Sb_5 . We observe a multitude of CDW-induced modes, whose symmetries and frequencies are in good agreement with DFT calculations for a single-layer CsV_3Sb_5 under inverse Star of David distortion. The observed temperature dependence of these modes and their calculated evolutions with varying lattice distortion allow us to identify two of them as amplitude modes, emerging from the predicted soft modes, although the soft modes are elusive experimentally. In contrast to mostly independent amplitude modes and zone-folded modes in well-known CDW materials^{44–46}, we show that they hybridize strongly in CsV_3Sb_5 , causing spectral weight redistribution to the latter and rendering them amplitude-mode-like. The anomalous hybridization and the large values of the amplitude mode frequencies provide evidence of strong-coupling CDW, offering a possible explanation for the

lack of soft modes. These results stress the importance of the lattice degree of freedom and electron–phonon coupling in the CDW formation in CsV_3Sb_5 .

Results

Raman-active modes in CsV_3Sb_5 . CsV_3Sb_5 crystallizes in a hexagonal lattice with the $P6/mmm$ space group¹¹. Figure 1b shows the unit cell of its crystal structure. The V atoms form a kagome net interspersed by Sb atoms (labeled Sb1), all within the ab -plane. The V atoms are further bonded by Sb atoms above and below the kagome plane (labeled Sb2). These V_3Sb_5 slabs are separated by Cs layers, with weak coupling between them to form a quasi-two-dimensional (quasi-2D) structure. Factor group analysis yields three Raman-active phonon modes, $\Gamma_{\text{Raman}} = A_{1g} + E_{2g} + E_{1g}$. The former two can be detected when the photons are polarized in the ab -plane, satisfied by the back-scattering geometry used in our experiment. These intense modes are marked by dashed lines in Fig. 1c, d. They involve only the Sb2 atoms, with their atomic vibrations along the c -axis and within the ab -plane for the A_{1g} and E_{2g} modes, respectively; see Fig. 1b. The E_{2g} modes are a pair of degenerate vibrations with opposite circling directions, i.e., opposite chiralities (see Supplementary Note 1). These two types of symmetries can be distinguished by polarization-resolved measurements. Specifically, the A_{1g} modes can be detected in the XX and LL polarization configurations, whereas the E_{2g} modes appear in the XX, XY, and LR configurations. Here, XX and XY represent collinear and cross-linear polarization for the incident and scattered photons, and LL and LR involve circularly polarized light with left (L) and right (R) helicity. A comparison of data in all four configurations is included in Supplementary Fig. 1.

Below T_{CDW} , multiple peaks emerge, highlighted by the dotted lines in Fig. 1c, d. Their origin will be discussed in the next sections. These modes are rather weak compared to the main lattice phonons. Their disappearance at 100 K suggests a close correlation with CDW formation. In contrast, many weak peak-like structures below 100 cm^{-1} lack temperature dependence, whose origin is unclear.

Figure 1e compares the observed Raman mode frequencies with those from DFT calculations for a single layer of CsV_3Sb_5 ²², considering two possible forms of lattice distortion, the Star of David (SD) and inverse Star of David (ISD, also referred to as trihexagonal) structures. Both of them show the same number of A_{1g} and E_{2g} modes, but with different ordering. Overall, the calculated ISD phonons agree much better with the experimental results, as shown in the figure and in Supplementary Tab. 1. All the five predicted A_{1g} modes and five out of the eight predicted E_{2g} modes are observed. The observed A_{1g} mode below 50 cm^{-1} is unaccounted for by our calculations. This mode was also observed by pump-probe time-resolved spectroscopy, which, when compared with calculations taking into account interlayer coupling, was assigned as a Cs-mode due to CDW modulation along the c -axis²³. Except for this mode and the three missing E_{2g} modes due to their weak scattering cross section, the symmetry ordering of all the other modes is in exact agreement between the experiment and theory. These results suggest that the CDW ground state consists of weakly coupled layers dominated by ISD-type distortion, but CDW modulation along the c -axis is also indispensable. Since the single-layer CsV_3Sb_5 holds the key to unraveling the CDW mechanism, we attempted creating atomically thin CsV_3Sb_5 by mechanical exfoliation. However, the loss of crystallinity impeded further investigation (Supplementary Figs. 2 and 3). The almost non-detection of modes folded from the L -point may be attributed to weak interlayer interaction, because the M - and L -point instabilities differ only in the

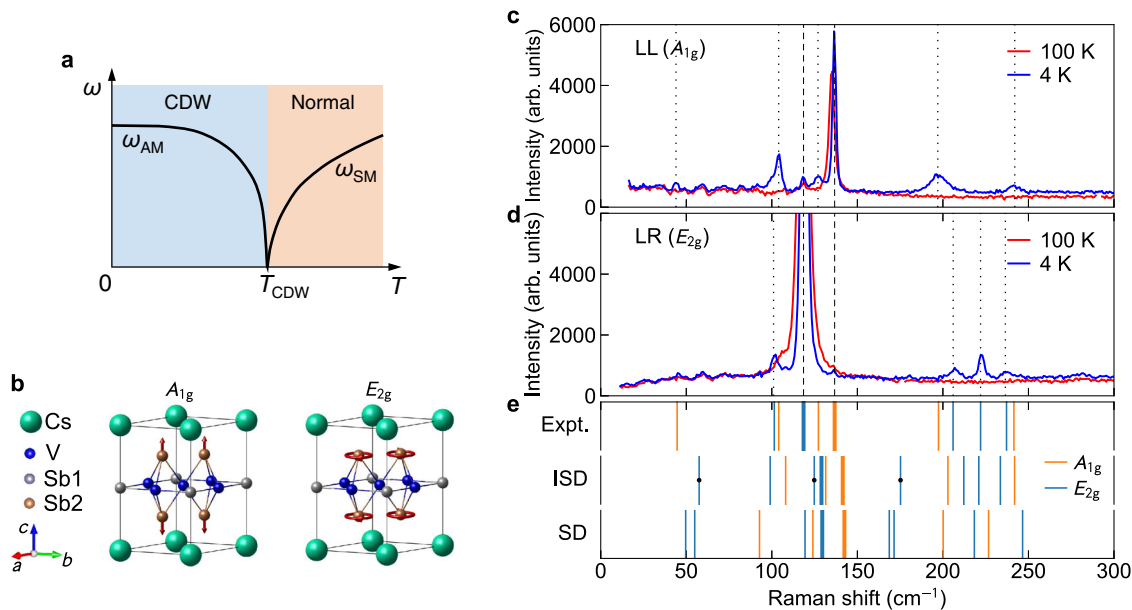


Fig. 1 Raman-active phonon modes in CsV_3Sb_5 . **a** Schematic illustration of the relation between the soft mode and amplitude mode in typical CDW materials, showing the latter emerges after the former freezes below T_{CDW} . ω_{AM} : amplitude mode frequency. ω_{SM} : soft mode frequency. **b** Crystal structure of CsV_3Sb_5 . Sb sites with different Wyckoff positions are labeled as Sb1 and Sb2. The arrows illustrate the vibration patterns of the main lattice A_{1g} and E_{2g} modes. The E_{2g} mode is doubly degenerate, and only one form is shown. **c, d** Raman spectra measured on the ab -plane at 100 K and 4 K in the LL and LR polarization configurations. The dashed lines denote the main lattice phonons, and the dotted lines indicate the CDW-induced modes. **e** Comparison of the measured (Expt.) and the calculated Raman mode frequencies for the inverse Star of David (ISD) and Star of David (SD) lattice distortions. The thick lines denote the main lattice phonons. The dots indicate modes undetected in our experiment.

interlayer ordering. Indeed, we have considered various forms of c -axis modulation, and all of them predict a large number of Raman modes far exceeding that observed experimentally (Supplementary Note 2). Polarization-angle dependent measurements (Supplementary Fig. 4) show that either the c -axis modulation is too weak to induce clear anisotropic Raman response, or those candidate stacking orders with the D_{2h} point group can be ruled out.

Temperature dependence of Raman modes. Figure 2a, b shows the temperature-dependent Raman intensity color plot for CsV_3Sb_5 , obtained in the LL and LR configurations, respectively. The intense A_{1g} and E_{2g} main lattice modes are the most conspicuous features. Figure 2e–g shows the frequency (with the corresponding value at 200 K subtracted), linewidth (full width at half maximum), and normalized integrated area for both modes, extracted from Lorentzian fits of the peaks. The A_{1g} frequency sharply increases below T_{CDW} , whereas the E_{2g} frequency exhibits a subtle kink across the CDW transition. This is consistent with the planar ISD lattice distortion mainly involving V atoms, forcing the Sb2 atoms to displace along the c -axis, hence affecting the out-of-plane vibration of the A_{1g} mode more effectively. The calculated phonon vibration patterns and frequencies confirm this picture (see Supplementary Fig. 5 and Supplementary Table 1). The CDW transition also causes a faster decrease in the linewidths below T_{CDW} . This can be understood as being due to the CDW-induced partial gapping of the Fermi surface^{33–37}, which reduces the electron–phonon interaction. The integrated peak intensity for both phonons increases upon warming, in line with increased thermal phonon populations. The rate of increase is faster when approaching T_{CDW} from below, and interestingly, the value saturates below approximately 50 K. The renormalization of the phonon parameters across the CDW transition evidences sizable electron–phonon coupling.

CDW-induced modes are labeled in Fig. 2a, b. Except for the A_1 mode, there appears to be two types of modes, represented by A_2 and E_3 . A_2 exhibits appreciable softening and broadening upon warming toward T_{CDW} . It is overdamped before disappearing, visualized in the color plot in Fig. 2a as the streak of signal below 100 cm^{-1} between 60 and 90 K (see also Supplementary Fig. 6). These are signatures of a CDW amplitude mode^{43–47}, caused by the collapse of coherent CDW order near T_{CDW} . E_3 shows a smaller change of frequency and much less broadening, more consistent with the characteristics of a zone-folded mode⁴⁴, as this type of mode arises from folding a zone-boundary phonon to the zone center, making its temperature dependence of the frequency as weak as that of normal phonons. Figure 2c, d compares the distinct temperature dependence of these two types of modes. While A_2 broadens significantly above 40 K, E_3 maintains its linewidth and suddenly vanishes above ~ 80 K. The dramatic difference in the linewidth broadening is quantified in Fig. 2i. Figure 2h shows the frequencies of all the observed Raman modes on the same scale. Upon warming, the CDW-induced modes (A_1 excluded) soften more dramatically than the main lattice modes. While it is tempting to assign most of them as amplitude modes because of the apparent softening behavior, we show below that they are in fact zone-folded modes, mixed with the amplitude modes to partially inherit their properties.

Nature of CDW-induced modes. Although soft phonons were not detected experimentally, our DFT results show that the formation of CDW in CsV_3Sb_5 is similar to that in other well-known systems^{43–47}, in the sense that a soft phonon mode at the CDW wavevector condenses and gives rise to a distorted lattice⁴¹. The imaginary phonon modes of pristine CsV_3Sb_5 at three M points (see Supplementary Fig. 7) transform as irreducible representation M_1^+ (A_g) of the space group $P6/mmm$ (little co-group D_{2h}). Figure 3a shows that they form triply degenerate modes at Γ due to the artificial band folding without lattice distortion, in which these modes are not

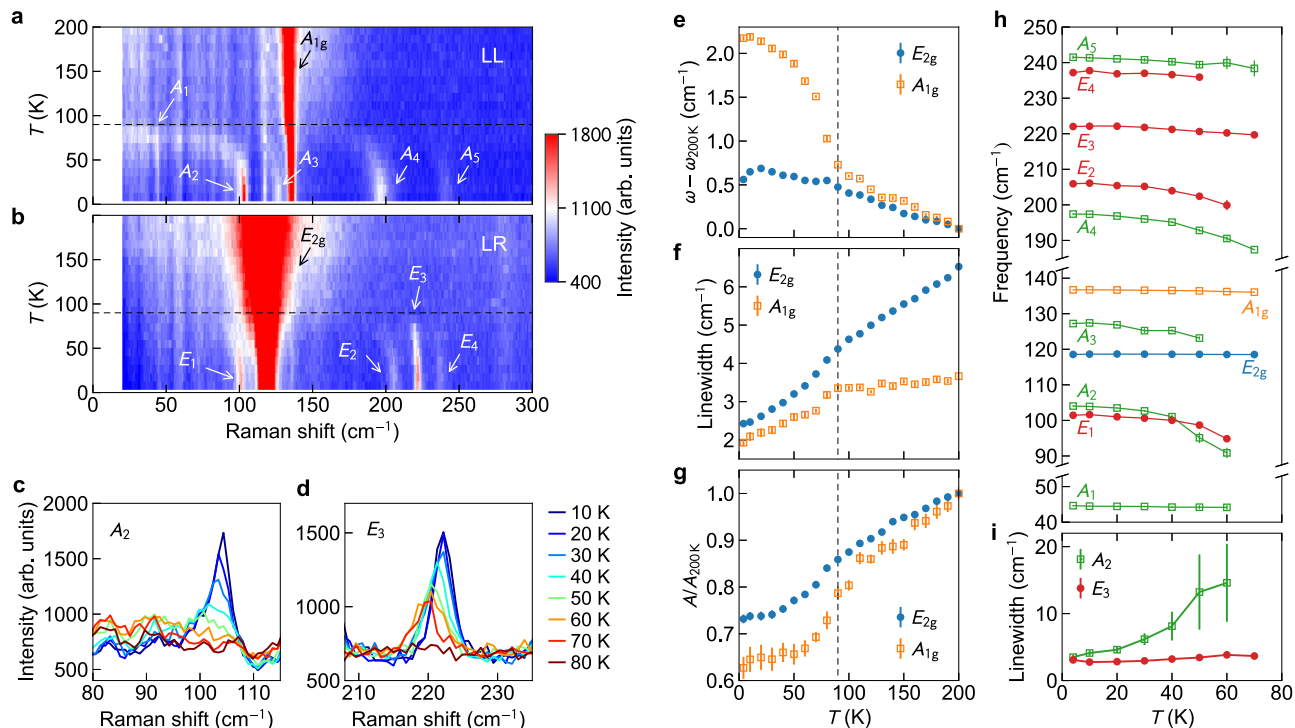


Fig. 2 Evolution of the Raman modes in CsV₃Sb₅ across the CDW transition. **a, b** Temperature-dependent Raman intensity color plot for CsV₃Sb₅, measured in the LL and LR configurations. The normal phonon modes are labeled in black and the CDW-induced modes in white. The dashed lines mark T_{CDW} . **c, d** Temperature-dependent spectra for the A_2 and E_3 modes. **e-g** Frequency, linewidth, and amplitude for the E_{2g} and A_{1g} main lattice phonons. The frequency and amplitude are compared to the corresponding values at 200 K. **h** Temperature dependence of the Raman mode frequencies. **i** Temperature dependence of the linewidth of the A_2 and E_3 modes. Error bars are standard deviations obtained from the least-squares fits to the phonon peaks.

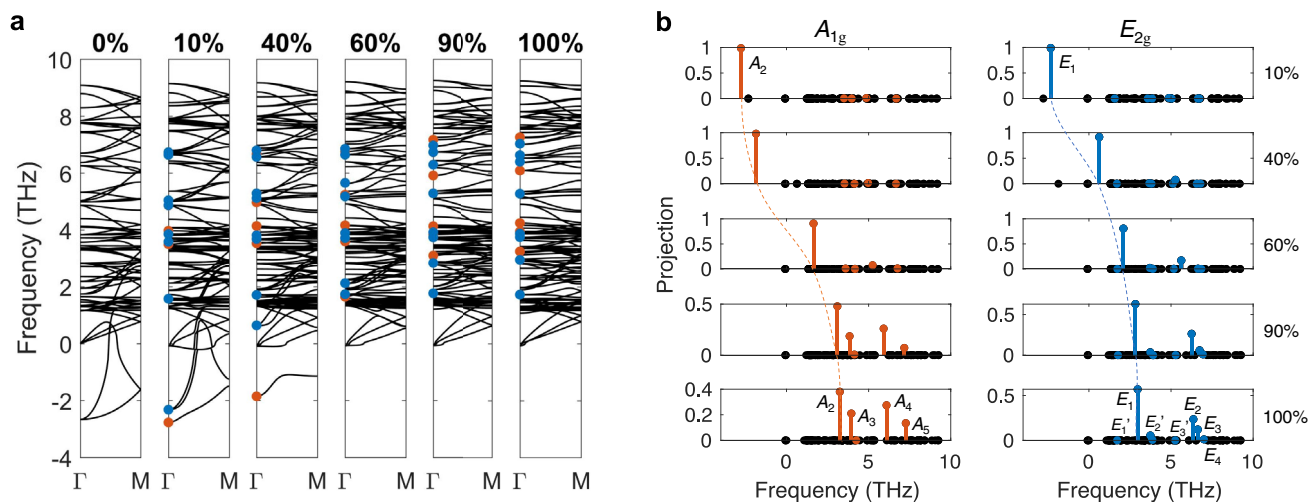


Fig. 3 Phonon band structures and mode mixing in the process of CDW distortion. **a** Phonon band structures directly calculated by DFT. Here, 100% (0%) refers to the fully stable ISD (2×2 pristine) structure. 10% refers to the intermediate structure with 10% distortion from the pristine to ISD phases. After $2 \times 2 \times 1$ band folding with no distortion, three imaginary modes (M_1^+) are folded to Γ . A weak ISD-type distortion lifts the degeneracy and leads to A_{1g} and E_{2g} modes. The ISD distortion gradually transforms imaginary modes to real. **b** Projections of the imaginary A_{1g} (E_{2g}) mode with 10% distortion to all the other phonon modes at Γ , as evolving into the stable ISD phase (100%). We highlight all A_{1g} and E_{2g} modes by orange and blue dots, respectively, at the Γ point. The dashed orange (blue) curve in **(b)** guides eyes to show the evolution of the imaginary A_2 (E_1) modes in the CDW distortion.

measurable in Raman. Only when CDW appears, they come out as amplitude modes, characterizing the CDW transition. With CDW distortion, they decompose to a singlet A_{1g} mode and a doublet E_{2g} mode under the point group D_{6h} (see Supplementary Note 3):

$$3M_1^+ \rightarrow A_{1g} \oplus E_{2g}. \quad (1)$$

Despite that intermediate structures in Fig. 3 are unstable structures with finite atomic forces, calculated force constants are still valid in the harmonic approximation (see “Methods”). Corresponding pseudo-phonon bands can provide useful insights to understand the soft mode evolution with respect to CDW distortion. As the lattice distorts from the pristine phase to the

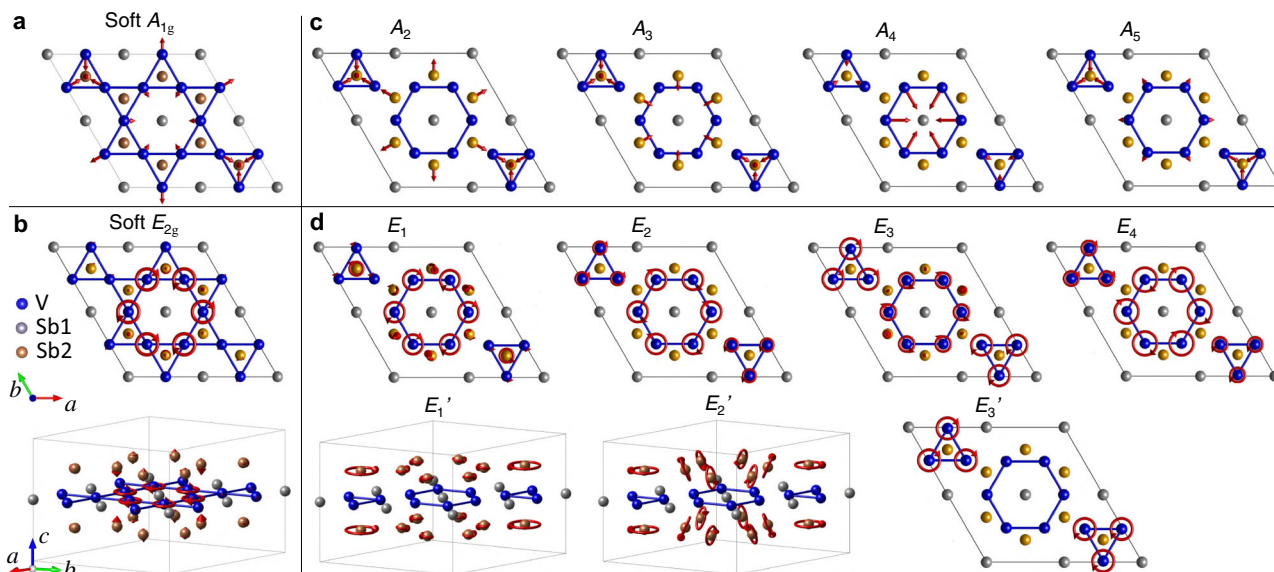


Fig. 4 Real space displacement patterns of the imaginary soft modes and the stable CDW-induced Raman modes in the $2 \times 2 \times 1$ ISD phase. **a, b** Soft modes with A_{1g} and E_{2g} symmetries, respectively. **c, d** CDW-induced A_{1g} and E_{2g} stable modes. The E_{2g} modes are pairs of chiral phonons and only one chiral mode is shown. The radius of the circles represents the amplitude of the vibration, and the arrow on the circles stands for the initial phase of the vibration. Cs atoms are omitted in the crystal structure for clarity, because they do not contribute to lattice vibrations.

stable ISD pattern, the imaginary A_{1g} and E_{2g} modes turn real with positive frequencies, expected to be observable as two Raman-active amplitude modes. The phonon displacement patterns of the soft A_{1g} and E_{2g} modes are shown in Fig. 4a, b, dominated by vibrations of V atoms. The A_{1g} mode is fully symmetric, involving breathing-type motion for the V triangles, V hexagons, and Sb2 atoms. The E_{2g} mode involves circling motion for the atoms forming the V hexagons, while the amplitude for the Sb2 vibration is almost ten times smaller.

DFT calculations further reveal that the amplitude modes strongly hybridize with the other CDW-induced Raman modes (i.e., the zone-folded modes always at positive frequencies at the Γ point in Fig. 3a), rendering them amplitude-mode-like, hence their apparent temperature-dependent frequencies. Figure 4c, d shows the real space displacement patterns of all the CDW-induced modes in the $2 \times 2 \times 1$ ISD phase. A_{2-5} and E_{1-4} correspond to those in Fig. 2, and E'_{1-3} are undetected experimentally. Comparison with Fig. 4a, b shows that A_{2-5} (E_{1-4}) all resemble the A_{1g} (E_{2g}) soft mode, but the difference is also apparent. The similarity results from hybridization of phonon modes.

To quantify the mode mixing, we calculated the overlap between the soft modes and all the real modes of the stable ISD phase by projecting the phonon dynamical matrix eigenvectors, $P_f = |\langle \mathbf{u}_f | \mathbf{u}_{SM} \rangle|^2$, where $|\mathbf{u}_{SM}\rangle$ refers to the eigenvector of the soft modes shown in Fig. 4a, b and $|\mathbf{u}_f\rangle$ refers to the eigenvector of the mode at frequency f in the ISD phase. The results in Fig. 3b show that as the soft A_{1g} and E_{2g} modes shift from negative to positive frequencies and turn into amplitude modes, they hybridize with most of the zone-folded modes belonging to the same irreducible representation. The amount of calculated projection in the stable ISD phase correlates reasonably well with the observed mode intensity in Fig. 1c, d. A_2 and E_1 are residual amplitude modes after mode mixing. E'_{1-3} show minor projection from the E_{2g} soft mode because of negligible eigenvector overlap, and accordingly their scattering cross section is weak. E_{2-4} all involve V triangles (Fig. 4d), indicating that they have contributions unrelated with the E_{2g} soft mode. Indeed, as discussed earlier, E_3 shows clear experimental signatures of a zone-folded mode.

The A_2 mode was also observed by Wulferding et al. in their Raman study⁵⁰ and by time-resolved pump-probe spectroscopy^{23,51}. However, in these works, it was suggested to emerge below ~ 60 K^{23,50,51}, hence ascribed to another phase transition associated with a unidirectional order^{19,25–27}. According to our data (Fig. 2a), the A_2 mode survives above 60 K, and there is no clear evidence for two distinct phase transitions. Its vibration pattern shown in Fig. 4c confirms no relation with the unidirectional order. Raman scattering, as a bulk probe, is probably not sensitive enough to the unidirectional order, due to its possible surface origin^{26,52} and its existence in nanoscale domains²⁶. A second bulk transition well below T_{CDW} was recently revealed by multiple techniques^{53–55}, which evaded detection by our Raman measurements, possibly also due to the lack of sufficient sensitivity. Another Raman study by Wu et al.⁵⁶ reported a similar set of modes as ours, but with different relative intensities. They also observed extra modes that are possibly due to stronger c -axis modulation in their sample.

Discussion

The anomalously large hybridization between the amplitude modes and zone-folded modes is rare, because they are mostly decoupled in the canonical CDW materials, with the amplitude modes dominating the spectral intensity^{44–46}. The hybridization is highly unusual, because the A_2 and E_1 amplitude modes and the zone-folded Raman modes span a wide frequency range, and they do not overlap in energy (except for E_1 and E'_1) to exhibit the typical anti-crossing^{57,58}. Their strong coupling suggests that the hybridization occurs indirectly, through interaction with the common electronic system. As the Fermi surface instability associated with the van Hove singularity is from the V bands²², modes mainly involving V (including A_{2-5} and E_{1-4}) naturally mix with the amplitude modes, whereas those mainly involving Sb (including E'_{1-2} and the A_{1g} and E_{2g} main lattice modes) do not. Similar mode mixing was also observed in the quasi-one-dimensional (quasi-1D) $K_{0.3}MoO_3$ using time-resolved pump-probe spectroscopy⁵⁹, and a simple model based on Ginzburg–Landau theory can well describe the entanglement of the electronic and lattice parts of the CDW order parameter. The similar phenomena observed in two systems with different

dimensionality suggest the importance of electron–phonon coupling in both materials.

However, a soft phonon is well established in $K_{0.3}MoO_3$ ⁶⁰, but shown to be absent in CsV_3Sb_5 ^{20,21}. In the mean-field weak-coupling theory^{28,41}, the phonon softening, known as Kohn anomaly⁶¹, is a direct consequence of the divergent electronic susceptibility, which screens the phonon vibration at the CDW wavevector. In reality, the singular electronic susceptibility is smeared out, especially at dimensions higher than one, and momentum dependent electron–phonon coupling dictates the phonon renormalization in certain systems such as $2H-NbSe_2$ ^{62,63}. The lack of soft phonons in CsV_3Sb_5 seems to rule out both mechanisms. Instead, CsV_3Sb_5 may fall into the strong electron–phonon coupling regime⁶⁴, in which the non-detection of Kohn anomaly in the quasi-1D $(TaSe_4)_2I$, $NbSe_3$, and $BaVS_3$ has also been reported^{65–67}. In all these materials, strong electron–phonon coupling tends to localize electrons, violating the adiabatic Born-Oppenheimer approximation⁶⁴ used in DFT. Failure of the conduction electrons to screen the phonon vibration can naturally explain the absence of phonon softening⁶⁸. Possible phonon softening is also interrupted by the first-order nature of the CDW transition^{53,69,70}, precluding the observation of complete softening to zero frequency. The first-order transition may be understood as due to trilinear coupling of the three components (3Q) of the CDW²⁴ or the asymmetric double-well elastic potential for the ions²², both contributing a term to the Landau free energy which is odd in the order parameter.

The strong-coupling nature of the CDW in CsV_3Sb_5 is indeed supported by multiple facts, according to the qualitative criteria discussed in ref. ²⁸. The CDW-induced gap Δ_{CDW} is large, with $2\Delta_{CDW}/k_B T_{CDW} \approx 22$ according to infrared spectroscopy³³, where k_B is the Boltzmann constant. The lattice distortion is substantial (amounting to about 5% of the lattice constant²²), the distorted lattice exhibits clustering of V atoms to form trimers and hexamers, and the CDW locks with the pristine lattice to form a commensurate structure, all indicating local chemical bonding^{22,38}. Moreover, DFT shows that the elastic potential for the ions in the pristine structure features double minima deeper than the thermal energy $k_B T_{CDW}$ at the transition²², a defining feature of the strong-coupling theory proposed by Gor'kov⁶⁴. Such potential well traps the ions in one of its minima, precluding soft phonon condensation. From the perspective of Raman scattering, the electron–phonon coupling constant λ can be estimated from the amplitude mode frequency ω_{AM} and the unscreened soft mode frequency ω_{SM}^0 as $\lambda = (\omega_{AM}/\omega_{SM}^0)^2$, valid on the mean-field level⁴¹. The results for CsV_3Sb_5 and a variety of other CDW materials are compiled in Fig. 5. Notably, the four quasi-2D compounds $2H-NbSe_2$, $2H-TaSe_2$, CsV_3Sb_5 , and $1T-TiSe_2$ are roughly located in the expected order according to their T_{CDW} , Δ_{CDW} , and commensurability. The frequencies of the amplitude modes in CsV_3Sb_5 are large, only lower than that of the higher one in $1T-TiSe_2$. Although the exact value of λ may not be meaningful beyond the weak-coupling limit, these results clearly indicate the strong-coupling nature of the CDW in CsV_3Sb_5 .

Our Raman results offer informative insights into the CDW phase in CsV_3Sb_5 , suggesting the dominance of the ISD-type distortion revealed by the CDW-induced modes and evidencing strong electron–phonon coupling. Although these results favor the local chemical bonding picture of the CDW transition, a coherent understanding of the mechanism, which should reconcile with the evidence for the electronically-driven scenario^{22,30–37}, is apparently called for. CsV_3Sb_5 represents a unique case in which the amplitude modes emerge in the

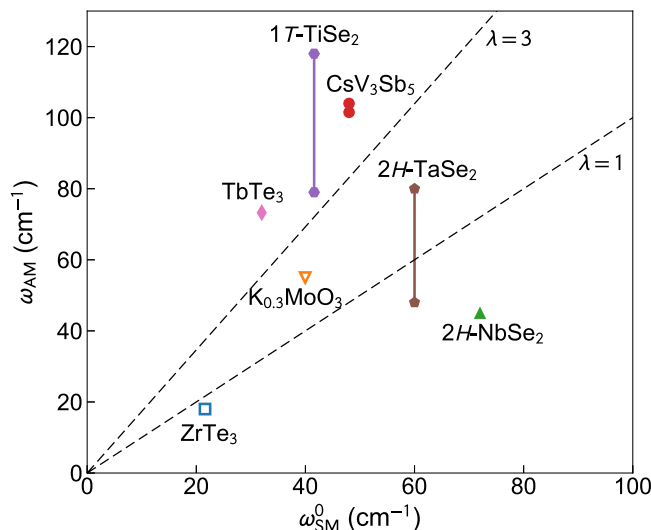


Fig. 5 Evidence of strong-coupling CDW in CsV_3Sb_5 . Frequency of the amplitude mode ω_{AM} in the zero-temperature limit and the unscreened frequency of the soft mode ω_{SM}^0 far above T_{CDW} for a collection of CDW materials. Some of the materials feature two amplitude modes, hence two data points connected by a vertical line. Since no soft mode is observed in CsV_3Sb_5 , ω_{SM}^0 is taken to be its acoustic phonon frequency at 300 K²¹. Open (filled) symbols indicate the material is quasi-1D (quasi-2D). The dashed lines mark electron–phonon coupling constant $\lambda = 1$ and 3 according to mean-field theory. Source of data: $ZrTe_3$ ^{80,81}, $TbTe_3$ ^{57,82}, $K_{0.3}MoO_3$ ^{43,60}, $1T-TiSe_2$ ^{47,83}, $2H-TaSe_2$ ^{45,46,84}, $2H-NbSe_2$ ^{84–86}.

absence of soft phonons. As important collective excitations of the CDW ground state, how they form without being driven by folding of a soft phonon warrants further investigation. DFT accurately predicts the CDW-induced Raman modes in the zero-temperature limit, meanwhile showing the typical correlation of the amplitude modes and soft modes illustrated in Fig. 1a, suggesting that the experimentally elusive soft mode is somehow still relevant. Our work may stimulate further studies of the interplay between CDW amplitude modes and possible superconducting Higgs mode^{48,49,71} in the kagome metals and the control of these symmetry-breaking states by ultrafast light^{72–74}.

Methods

Sample preparation. CsV_3Sb_5 single crystals were synthesized using the flux method¹¹. The freshly cleaved surface of the samples was used in the study of bulk crystals. Raman scattering spectroscopy was performed using home-built confocal microscopy setups in the back-scattering geometry with 532 nm laser excitation. The normally incident light was focused on the sample to a micron-sized spot, and the scattered light was directed through Bragg notch filters to access the low-wavenumber region. The Raman signal was collected using a grating spectrograph and a liquid-nitrogen-cooled charge-coupled device. The samples were mounted in a vacuum chamber during data acquisition. Temperature control was achieved using a Montana Instrument Cryostation.

Calculations. The DFT calculation results by Tan et al.²² are used to compare with the experiment. In addition, we calculated the force constants by Vienna ab-initio Simulation Package (VASP)⁷⁵ and computed the phonon dispersion relation by Phonopy⁷⁶. Perdew–Burke–Ernzerhof-type generalized gradient approximation (GGA) method has been used⁷⁷ and the projected augmented wave (PAW) potentials with 9 valence electrons for the Cs atom, 5 valence electrons for V and Sb atoms are employed. The DFT-D3 correction⁷⁸ is used to take interlayer van der Waals interactions into account. For the DFT calculation, a $5 \times 5 \times 5k$ mesh and an energy cutoff of 400 eV were used. For the pseudo-phonon spectra of the intermediate structures in Fig. 3, we used the same frozen phonon method to calculate force derivatives and obtained force constants, which is valid in the harmonic approximation. Specifically, for each intermediate structure we calculated the force differences between the slightly perturbed structure and the unperturbed one. The

representation decomposition relation in Eq. (1) is derived by directly calculating the characters of the folded modes (whose real space patterns are shown in Supplementary Fig. 7). See more details in Supplementary Note 3. The symmetry representations of Raman-active modes are calculated using the methods in ref. ⁷⁹ as implemented in Bilbao Crystallographic Server.

Data availability

The data in Figure 1e are provided in Supplementary Table 1. Other data are available from the corresponding authors upon reasonable request.

Received: 26 February 2022; Accepted: 3 June 2022;

Published online: 16 June 2022

References

- Sachdev, S. Kagomé- and triangular-lattice Heisenberg antiferromagnets: Ordering from quantum fluctuations and quantum-disordered ground states with unconfined bosonic spinons. *Phys. Rev. B* **45**, 12377–12396 (1992).
- Han, T.-H. et al. Fractionalized excitations in the spin-liquid state of a kagome-lattice antiferromagnet. *Nature* **492**, 406–410 (2012).
- Mazin, I. I. et al. Theoretical prediction of a strongly correlated Dirac metal. *Nat. Commun.* **5**, 4261 (2014).
- Ye, L. et al. Massive Dirac fermions in a ferromagnetic kagome metal. *Nature* **555**, 638–642 (2018).
- Tang, E., Mei, J.-W. & Wen, X.-G. High-temperature fractional quantum Hall states. *Phys. Rev. Lett.* **106**, 236802 (2011).
- Xu, G., Lian, B. & Zhang, S.-C. Intrinsic quantum anomalous Hall effect in the kagome lattice $\text{Cs}_2\text{LiMn}_3\text{F}_{12}$. *Phys. Rev. Lett.* **115**, 186802 (2015).
- Kang, M. et al. Topological flat bands in frustrated kagome lattice CoSn . *Nat. Commun.* **11**, 4004 (2020).
- Yu, S.-L. & Li, J.-X. Chiral superconducting phase and chiral spin-density-wave phase in a Hubbard model on the kagome lattice. *Phys. Rev. B* **85**, 144402 (2012).
- Kiesel, M. L., Platt, C. & Thomale, R. Unconventional Fermi surface instabilities in the kagome Hubbard model. *Phys. Rev. Lett.* **110**, 126405 (2013).
- Wang, W.-S., Li, Z.-Z., Xiang, Y.-Y. & Wang, Q.-H. Competing electronic orders on kagome lattices at van Hove filling. *Phys. Rev. B* **87**, 115135 (2013).
- Ortiz, B. R. et al. New kagome prototype materials: discovery of KV_3Sb_5 , RbV_3Sb_5 , and CsV_3Sb_5 . *Phys. Rev. Mater.* **3**, 094407 (2019).
- Ortiz, B. R. et al. CsV_3Sb_5 : a \mathbb{Z}_2 topological kagome metal with a superconducting ground state. *Phys. Rev. Lett.* **125**, 247002 (2020).
- Liu, Z. et al. Charge-density-wave-induced bands renormalization and energy gaps in a kagome superconductor RbV_3Sb_5 . *Phys. Rev. X* **11**, 041010 (2021).
- Kang, M. et al. Twofold van Hove singularity and origin of charge order in topological kagome superconductor CsV_3Sb_5 . *Nat. Phys.* <https://doi.org/10.1038/s41567-021-01451-5> (2022).
- Ortiz, B. R. et al. Superconductivity in the \mathbb{Z}_2 kagome metal KV_3Sb_5 . *Phys. Rev. Mater.* **5**, 034801 (2021).
- Yin, Q. et al. Superconductivity and normal-state properties of kagome metal RbV_3Sb_5 single crystals. *Chin. Phys. Lett.* **38**, 037403 (2021).
- Yang, S.-Y. et al. Giant, unconventional anomalous Hall effect in the metallic frustrated magnet candidate, KV_3Sb_5 . *Sci. Adv.* **6**, eabb6003 (2020).
- Yu, F. H. et al. Concurrence of anomalous Hall effect and charge density wave in a superconducting topological kagome metal. *Phys. Rev. B* **104**, L041103 (2021).
- Chen, H. et al. Roton pair density wave in a strong-coupling kagome superconductor. *Nature* **599**, 222–228 (2021).
- Li, H. et al. Observation of unconventional charge density wave without acoustic phonon anomaly in kagome superconductors AV_3Sb_5 ($A = \text{Rb}, \text{Cs}$). *Phys. Rev. X* **11**, 031050 (2021).
- Xie, Y. et al. Electron-phonon coupling in the charge density wave state of CsV_3Sb_5 . *Phys. Rev. B* **105**, L140501 (2022).
- Tan, H., Liu, Y., Wang, Z. & Yan, B. Charge density waves and electronic properties of superconducting kagome metals. *Phys. Rev. Lett.* **127**, 046401 (2021).
- Ratcliff, N., Hallett, L., Ortiz, B. R., Wilson, S. D. & Harter, J. W. Coherent phonon spectroscopy and interlayer modulation of charge density wave order in the kagome metal CsV_3Sb_5 . *Phys. Rev. Mater.* **5**, L111801 (2021).
- Christensen, M. H., Biroli, T., Andersen, B. M. & Fernandes, R. M. Theory of the charge density wave in AV_3Sb_5 kagome metals. *Phys. Rev. B* **104**, 214513 (2021).
- Zhao, H. et al. Cascade of correlated electron states in the kagome superconductor CsV_3Sb_5 . *Nature* **599**, 216–221 (2021).
- Wang, Z. et al. Electronic nature of chiral charge order in the kagome superconductor CsV_3Sb_5 . *Phys. Rev. B* **104**, 075148 (2021).
- Liang, Z. et al. Three-dimensional charge density wave and surface-dependent vortex-core states in a kagome superconductor CsV_3Sb_5 . *Phys. Rev. X* **11**, 031026 (2021).
- Rosnagel, K. On the origin of charge-density waves in select layered transition-metal dichalcogenides. *J. Phys.: Condens. Matter.* **23**, 213001 (2011).
- Ortiz, B. R. et al. Fermi surface mapping and the nature of charge-density-wave order in the kagome superconductor CsV_3Sb_5 . *Phys. Rev. X* **11**, 041030 (2021).
- Lin, Y.-P. & Nandkishore, R. M. Complex charge density waves at van Hove singularity on hexagonal lattices: Haldane-model phase diagram and potential realization in the kagome metals AV_3Sb_5 ($A = \text{K}, \text{Rb}, \text{Cs}$). *Phys. Rev. B* **104**, 045122 (2021).
- Park, T., Ye, M. & Balents, L. Electronic instabilities of kagome metals: saddle points and Landau theory. *Phys. Rev. B* **104**, 035142 (2021).
- Denner, M. M., Thomale, R. & Neupert, T. Analysis of charge order in the kagome metal AV_3Sb_5 ($A = \text{K}, \text{Rb}, \text{Cs}$). *Phys. Rev. Lett.* **127**, 217601 (2021).
- Zhou, X. et al. Origin of charge density wave in the kagome metal CsV_3Sb_5 as revealed by optical spectroscopy. *Phys. Rev. B* **104**, L041101 (2021).
- Uykur, E. et al. Low-energy optical properties of the nonmagnetic kagome metal CsV_3Sb_5 . *Phys. Rev. B* **104**, 045130 (2021).
- Nakayama, K. et al. Multiple energy scales and anisotropic energy gap in the charge-density-wave phase of the kagome superconductor CsV_3Sb_5 . *Phys. Rev. B* **104**, L161112 (2021).
- Lou, R. et al. Charge-density-wave-induced peak-dip-hump structure and the multiband superconductivity in a kagome superconductor CsV_3Sb_5 . *Phys. Rev. Lett.* **128**, 036402 (2022).
- Luo, Y. et al. Distinct band reconstructions in kagome superconductor CsV_3Sb_5 . Preprint at <https://arxiv.org/abs/2106.01248> (2021).
- Wang, C., Liu, S., Jeon, H. & Cho, J.-H. Origin of charge density wave in the layered kagome metal CsV_3Sb_5 . *Phys. Rev. B* **105**, 045135 (2022).
- Ye, Z., Luo, A., Yin, J.-X., Zahid Hasan, M. & Xu, G. Structural instability and charge modulations in the Kagome superconductor AV_3Sb_5 . Preprint at <https://arxiv.org/abs/2111.07314> (2021).
- Rice, M. & Strässler, S. Theory of the soft phonon mode and dielectric constant below the Peierls transition temperature. *Solid State Commun.* **13**, 1931–1933 (1973).
- Grüner, G. *Density Waves in Solids*. Advanced book program: Addison-Wesley (Perseus Books Group, 2000).
- Sugai, S. Lattice vibrations in the charge-density-wave states of layered transition metal dichalcogenides. *Phys. Stat. Sol. B* **129**, 13–39 (1985).
- Travaglini, G., Mörke, I. & Wachter, P. CDW evidence in one-dimensional $\text{K}_0.3\text{MoO}_3$ by means of Raman scattering. *Solid State Commun.* **45**, 289–292 (1983).
- Joshi, J. et al. Short-range charge density wave order in $2H\text{-TaS}_2$. *Phys. Rev. B* **99**, 245144 (2019).
- Hill, H. M. et al. Phonon origin and lattice evolution in charge density wave states. *Phys. Rev. B* **99**, 174110 (2019).
- Lin, D. et al. Patterns and driving forces of dimensionality-dependent charge density waves in $2H$ -type transition metal dichalcogenides. *Nat. Commun.* **11**, 2406 (2020).
- Barath, H. et al. Quantum and classical mode softening near the charge-density-wave–superconductor transition of Cu_xTiSe_2 . *Phys. Rev. Lett.* **100**, 106402 (2008).
- Méasson, M.-A. et al. Amplitude Higgs mode in the $2H\text{-NbSe}_2$ superconductor. *Phys. Rev. B* **89**, 060503 (2014).
- Grasset, R. et al. Pressure-induced collapse of the charge density wave and Higgs mode visibility in $2H\text{-TaS}_2$. *Phys. Rev. Lett.* **122**, 127001 (2019).
- Wulferding, D. et al. Fermi surface instabilities in electronic Raman scattering of the metallic kagome lattice CsV_3Sb_5 . Preprint at <https://arxiv.org/abs/2108.11690> (2021).
- Wang, Z. X. et al. Unconventional charge density wave and photoinduced lattice symmetry change in the kagome metal CsV_3Sb_5 probed by time-resolved spectroscopy. *Phys. Rev. B* **104**, 165110 (2021).
- Li, H. et al. Spatial symmetry constraint of charge-ordered kagome superconductor CsV_3Sb_5 . Preprint at <https://arxiv.org/abs/2109.03418> (2021).
- Luo, J. et al. Possible star-of-David pattern charge density wave with additional modulation in the kagome superconductor CsV_3Sb_5 . *npj Quantum Mater.* **7**, 30 (2022).
- Nie, L. et al. Charge-density-wave-driven electronic nematicity in a kagome superconductor. *Nature* **604**, 59–64 (2022).
- Khasanov, R. et al. Charge order breaks time-reversal symmetry in CsV_3Sb_5 . Preprint at <https://arxiv.org/abs/2203.12317> (2022).
- Wu, S. et al. Charge density wave order in the kagome metal AV_3Sb_5 ($A = \text{Cs}, \text{Rb}, \text{K}$). *Phys. Rev. B* **105**, 155106 (2022).
- Yusupov, R. V., Mertelj, T., Chu, J.-H., Fisher, I. R. & Mihailovic, D. Single-particle and collective mode couplings associated with 1- and 2-directional

- electronic ordering in metallic $R\text{Te}_3$ ($R = \text{Ho, Dy, Tb}$). *Phys. Rev. Lett.* **101**, 246402 (2008).
58. Lavagnini, M. et al. Raman scattering evidence for a cascade evolution of the charge-density-wave collective amplitude mode. *Phys. Rev. B* **81**, 081101 (2010).
 59. Schäfer, H., Kabanov, V. V., Beyer, M., Biljakovic, K. & Demsar, J. Disentanglement of the electronic and lattice parts of the order parameter in a 1D charge density wave system probed by femtosecond spectroscopy. *Phys. Rev. Lett.* **105**, 066402 (2010).
 60. Pouget, J. P., Hennion, B., Escribe-Filippini, C. & Sato, M. Neutron-scattering investigations of the Kohn anomaly and of the phase and amplitude charge-density-wave excitations of the blue bronze $\text{K}_{0.3}\text{MoO}_3$. *Phys. Rev. B* **43**, 8421–8430 (1991).
 61. Kohn, W. Image of the Fermi surface in the vibration spectrum of a metal. *Phys. Rev. Lett.* **2**, 393–394 (1959).
 62. Johannes, M. D. & Mazin, I. I. Fermi surface nesting and the origin of charge density waves in metals. *Phys. Rev. B* **77**, 165135 (2008).
 63. Zhu, X., Cao, Y., Zhang, J., Plummer, E. W. & Guo, J. Classification of charge density waves based on their nature. *Proc. Natl Acad. Sci.* **112**, 2367–2371 (2015).
 64. Gor'kov, L. P. Strong electron-lattice coupling as the mechanism behind charge density wave transformations in transition-metal dichalcogenides. *Phys. Rev. B* **85**, 165142 (2012).
 65. Lorenzo, J. E. et al. A neutron scattering study of the quasi-one-dimensional conductor $(\text{TaSe}_4)_2\text{I}$. *J. Phys.: Condens. Matter* **10**, 5039–5068 (1998).
 66. Requardt, H., Lorenzo, J. E., Monceau, P., Currat, R. & Krisch, M. Dynamics in the charge-density-wave system NbSe_3 using inelastic x-ray scattering with meV energy resolution. *Phys. Rev. B* **66**, 214303 (2002).
 67. Ilakovac, V. et al. Order-disorder type of Peierls instability in BaVS_3 . *Phys. Rev. B* **103**, 014306 (2021).
 68. Pouget, J.-P. The Peierls instability and charge density wave in one-dimensional electronic conductors. *Comptes Rendus Physique* **17**, 332–356 (2016).
 69. Mu, C. et al. S-wave superconductivity in kagome metal CsV_3Sb_5 revealed by $^{121/123}\text{Sb}$ NQR and ^{51}V NMR measurements. *Chin. Phys. Lett.* **38**, 077402 (2021).
 70. Song, D. et al. Orbital ordering and fluctuations in a kagome superconductor CsV_3Sb_5 . *Sci. China-Phys. Mech. Astron.* **65**, 247462 (2022).
 71. Shimano, R. & Tsuji, N. Higgs mode in superconductors. *Ann. Rev. Condens. Matter Phys.* **11**, 103–124 (2020).
 72. Schmitt, F. et al. Transient electronic structure and melting of a charge density wave in TbTe_3 . *Science* **321**, 1649–1652 (2008).
 73. Zhang, Y. et al. Coherent modulation of the electron temperature and electron-phonon couplings in a 2D material. *Proc. Natl. Acad. Sci. USA* **117**, 8788–8793 (2020).
 74. Lloyd-Hughes, J. et al. The 2021 ultrafast spectroscopic probes of condensed matter roadmap. *J. Phys.: Condens. Matter* **33**, 353001 (2021).
 75. Kresse, G. & Furthmüller, J. Efficient iterative schemes for ab initio total-energy calculations using a plane-wave basis set. *Phys. Rev. B* **54**, 11169–11186 (1996).
 76. Togo, A. & Tanaka, I. First principles phonon calculations in materials science. *Scr. Mater.* **108**, 1–5 (2015).
 77. Perdew, J. P., Burke, K. & Ernzerhof, M. Generalized gradient approximation made simple. *Phys. Rev. Lett.* **77**, 3865–3868 (1996).
 78. Grimme, S., Antony, J., Ehrlich, S. & Krieg, H. A consistent and accurate ab initio parametrization of density functional dispersion correction (DFT-D) for the 94 elements H-Pu. *J. Chem. Phys.* **132**, 154104 (2010).
 79. Kroumova, E. et al. Bilbao crystallographic server: useful databases and tools for phase-transition studies. *Phase Transit.* **76**, 155–170 (2003).
 80. Hu, Y., Zheng, F., Ren, X., Feng, J. & Li, Y. Charge density waves and phonon-electron coupling in ZrTe_3 . *Phys. Rev. B* **91**, 144502 (2015).
 81. Hoesch, M., Bosak, A., Chernyshov, D., Berger, H. & Krisch, M. Giant Kohn anomaly and the phase transition in charge density wave ZrTe_3 . *Phys. Rev. Lett.* **102**, 086402 (2009).
 82. Maschek, M. et al. Wave-vector-dependent electron-phonon coupling and the charge-density-wave transition in TbTe_3 . *Phys. Rev. B* **91**, 235146 (2015).
 83. Weber, F. et al. Electron-phonon coupling and the soft phonon mode in TiSe_2 . *Phys. Rev. Lett.* **107**, 266401 (2011).
 84. Moncton, D. E., Axe, J. D. & DiSalvo, F. J. Study of superlattice formation in $2H\text{-NbSe}_2$ and $2H\text{-TaSe}_2$ by neutron scattering. *Phys. Rev. Lett.* **34**, 734–737 (1975).
 85. Weber, F. et al. Extended phonon collapse and the origin of the charge-density wave in $2H\text{-NbSe}_2$. *Phys. Rev. Lett.* **107**, 107403 (2011).
 86. Tsang, J. C., Smith, J. E. & Shafer, M. W. Raman spectroscopy of soft modes at the charge-density-wave phase transition in $2H\text{-NbSe}_2$. *Phys. Rev. Lett.* **37**, 1407–1410 (1976).

Acknowledgements

This work was supported by the National Key Research and Development Program of China (Grant Nos. 2018YFA0307000 and 2017YFA0303201) and the National Natural Science Foundation of China (Grant Nos. 11774151). Growth of hexagonal boron nitride crystals was supported by the Elemental Strategy Initiative conducted by the MEXT, Japan (Grant No. JPMXP0112101001), JSPS KAKENHI (Grant No. JP20H00354), and A3 Foresight by JSPS. B.Y. acknowledges the financial support by the European Research Council (ERC Consolidator Grant “NonlinearTopo”, No. 815869) and the ISF - Quantum Science and Technology (No. 1251/19).

Author contributions

X.X. conceived the project. G.L., X.M., and K.H. performed the Raman experiments. Q.L., Y.D., and H.-H.W. grew the CsV_3Sb_5 crystals. K.W. and T.T. grew the h-BN crystals. G.L. and X.X. analyzed the experimental data. H.T., Y.L., and B.Y. performed the DFT calculations. J.X., W.T., and L.G. performed atomic force microscopy measurements. X.X. and B.Y. interpreted the results and co-wrote the paper, with comments from all authors.

Competing interests

The authors declare no competing interests.

Additional information

Supplementary information The online version contains supplementary material available at <https://doi.org/10.1038/s41467-022-31162-1>.

Correspondence and requests for materials should be addressed to Binghai Yan or Xiaoxiang Xi.

Peer review information *Nature Communications* thanks the anonymous reviewers for their contribution to the peer review of this work. Peer reviewer reports are available.

Reprints and permission information is available at <http://www.nature.com/reprints>

Publisher's note Springer Nature remains neutral with regard to jurisdictional claims in published maps and institutional affiliations.



Open Access This article is licensed under a Creative Commons Attribution 4.0 International License, which permits use, sharing, adaptation, distribution and reproduction in any medium or format, as long as you give appropriate credit to the original author(s) and the source, provide a link to the Creative Commons license, and indicate if changes were made. The images or other third party material in this article are included in the article's Creative Commons license, unless indicated otherwise in a credit line to the material. If material is not included in the article's Creative Commons license and your intended use is not permitted by statutory regulation or exceeds the permitted use, you will need to obtain permission directly from the copyright holder. To view a copy of this license, visit <http://creativecommons.org/licenses/by/4.0/>.

© The Author(s) 2022